Journal of Materials Chemistry C

ROYAL SOCIETY OF CHEMISTRY

PAPER

View Article Online
View Journal | View Issue

Cite this: J. Mater. Chem. C, 2020, 8, 10844

Additive-controlled synthesis of monodisperse single crystalline gold nanoparticles: interplay of shape and surface plasmon resonance†

Felizitas Kirner,[a] Pavel Potapov,[b] Johannes Schultz,[b] Jessica Geppert,[a] Magdalena Müller,[a] Guillermo González-Rubio,[a] Sebastian Sturm,[b] Axel Lubk[b] and Elena Sturm *[a]

Received 7th April 2020,
Accepted 6th May 2020

DOI: 10.1039/d0tc01748e

rsc.li/materials-c

We introduce a three-step seed-mediated synthesis for single crystalline gold nanoparticles (Au NPs) stabilized by hexadecylpyridinium chloride (CPC) in variable sizes with an independently adjustable ratio of the cubic and octahedral facets. The effect of KBr and ascorbic acid (AA) on shape and growth kinetics is systematically investigated. The kinetic data were evaluated using the minimalistic Finke–Watzky autocatalytic two-step mechanism, which allows to estimate the rate constants of the "pseudoelementary" reactions. The proposed surface-mediated mechanism of reduction of gold ions and Au NP growth allows to explain the effect of gradual increase of bromide ion concentration on switching the Au NP morphology from cubic to octahedral. The plasmonic properties of single particles of different facetings and their assemblies are investigated.

Introduction

Nanoparticles are highly promising for a multitude of applications due to their unique physical properties (*e.g.* optical, magnetic, electronic, *etc.*) which can significantly differ from the properties of the bulk material. Gold nanoparticles (Au NPs) attract a special interest based on their optical properties related to localized surface plasmons.

The plasmonic behavior of metallic nanoparticles is highly responsive to extrinsic factors (physical–chemical environment, dielectric constant, temperature, interactions of particles, stabilizing agent, *etc.*) and their morphology (size, shape, quality of surface). A change of the plasmonic behavior in response to a variation of the environment makes Au NPs an excellent sensor material for a huge range of applications such as Surface-enhanced Raman spectroscopy (SERS)[1,2] toxic metal ion detection,[3] food safety screening,[4] and medical diagnosis.[5–7] The assembly of spherical Au NPs even allows the tuning of their collective plasmon mode from the visible through the near-infrared region,[1] therefore they can potentially be used for constructing metamaterials.[8,9] Electrocatalysis is another possible application for faceted gold nanocrystals.[10,11] Intrinsic changes of the particle morphology and size offer even more possibilities to control the plasmonic behavior and tune the resonance wavelength to specific applications.[12–14] Note furthermore that the surface quality of Au NPs is typically superior to lithographically fabricated Au nanostructures, favorably affecting Au NP based plasmonic applications in terms of loss and quality factors.[15]

Bottom-up synthesis of nanomaterials with controlled structures and elaborate functionalities is always a conceptual challenge in nanotechnology and material sciences.[16,17] It consists of two steps, the synthesis of high-quality monodisperse NPs of controlled size, shape and composition, and the assembly of these into well-ordered arrays (*i.e.* superlattices).

Many different synthesis routes have been explored to achieve monodisperse nanoparticles with defined shape. Anisotropic Au NPs in organic solvents are commonly synthesized using the so-called "polyol process". The fundamental parameters involved are not yet identified, which hinders a rational nanoparticle design.[18] The synthesis of anisotropic Au NPs in water was developed significantly earlier. Using citrate as a reducing and stabilizing agent can certainly lead to a wide range of sizes with defined size distributions, a shape control however is virtually non-existent.[19,20]

Syntheses that yield shape-controlled nanoparticles vastly follow a seed-mediated growth method[21] and allow the size control of nanoparticles by changing the seed to gold salt ratio. Small gold particles are produced by a harsh reduction of Au

[a] Department of Chemistry, University of Konstanz, Universitätsstr. 10, D-78457 Konstanz, Germany. E-mail: elena.sturm@uni-konstanz.de
[b] Institute for Solid State Research, Leibniz Institute for Solid State and Materials Research Dresden, Helmholtzstraße 20, 01069 Dresden, Germany

† Electronic supplementary information (ESI) available: Details of reaction parameters; synthesis and characterization of seed particles; procedure for the measurement and evaluation of the growth kinetics of NPs; Table S1 and Fig. S1–S15. See DOI: 10.1039/d0tc01748e

ions in presence of high supersaturation. These gold particles are subsequently used as seeds for the growth of larger crystals under milder conditions. CTAB (cetyltrimethylammonium bromide) is typically used as surface-active agent in seed-mediated syntheses of single crystalline gold nanocrystals.[22,23]

Gold nanorod synthesis follows the most established protocols that reproducibly allow a high degree of control over both size and aspect ratio.[18,24,25] Synthesis of platonic nanoparticles is especially interesting due to their defined faceting with congruent faces and the same number of faces meeting at each vertex. Dodecahedra and icosahedra can never be synthesized single crystalline due to symmetry constrictions. A tetrahedron displays different, non-isotropic facets and is therefore hard to synthesize. Cubes and octahedra and the according Archimedean solids (rhombicuboctahedra) are interesting due to their symmetry of facets and predictable packing behavior.

The CTAB surfactant is known to alter the surface energies of naked gold facets as the surfactant layer preferably covers {100} and {110} facets and leaves the {111} facets less protected. These facets are then more accessible for growth in this direction.[10,26] In the growth process it is reported that cubic particles are obtained in high yield using low CTAB concentrations and low ascorbic acid (AA) concentrations while octahedra are obtained in syntheses with high CTAB and high AA concentrations.[18,24,27–29]

CTAB-dependent syntheses are known to be highly influenced by batch-to-batch varying impurities contained in the CTAB. Gold nanocrystals with different faceting but defined size can be synthesized by using specific CTAB batches.[26,30–33] This is commonly attributed to traces of halides remaining in the CTAB after the manufacturing process.[26,32–34] Nonetheless, crystal shapes such as cubes,[29] rods,[24,35] octahedra[29,36] and stars[37,38] are reported in literature. Under the aspect of reproducibility, this still poses a huge problem.

There are approaches to overcome this issue by changing the surfactant. Niu *et al.*[23] present a method where they use etched rods as seed particles for the growth process with hexadecylpyridinium chloride (CPC) as surfactant. Cubes grown with this method show quite broad average edge lengths. O'Brien *et al.*[23,39] overcome this issue by a repeated etching and overgrowth process of rods to yield spherical particles. The loss during this process is quite high and they need to adjust reaction parameters for each synthesis batch individually. Therefore, this procedure is quite time consuming and requires lots of analytical investigation before the actual growth. It was stated that the proposed synthesis procedure yields particles with the same faceting in different sizes by changing only the number of seeds. In addition, a strong adaption of the synthesis protocol to desired shape is required. It is proposed that octahedral nanocrystals are formed due to the strong adsorption of CPC molecules capping the octahedral {111} facets, while the cubic {100} facet is preferably developed in the final shape when bromide ions are present.[23] However, this study does not provide a systematic investigation of the influence of the bromide and AA concentration on the morphology of Au NPs.

Here we present a fast and easy method for the synthesis of monodisperse single crystalline gold nanoparticles with sizes between 26 nm and 100 nm. The influence of bromide and AA concentrations on the ratio of the cubic {100} and the octahedral {111} facets in the final shape of the NPs is systematically investigated leading to steplessly tunable habits. The growth kinetic of particles of different size and morphologies is investigated using UV-Vis spectroscopy. The kinetic data were evaluated using the adjusted Finke–Watzky (FW) autocatalytic two–step mechanism which allows to estimate the rate constants of the ''pseudoelementary'' reactions of reduction of gold ions and growth process of NPs with different shape.[40–45] The proposed surface-mediated mechanism of the reduction of gold ions and the Au NP growth allows to explain the effect of gradual increase of bromide ion concentration on switching the Au NP morphology from cubic to octahedral. Furthermore, the plasmonic response of grown NPs of different habits is investigated and their utility in manufacturing nanostructures with the desired plasmonic properties is demonstrated.

Materials and methods

Chemicals and materials

Milli-Q water (resistivity 18.2 MΩ cm) was used in all experiments. All chemicals were bought and used as received. Hydrogen tetrachloroaurate trihydrate ($HAuCl_4 \cdot 3H_2O$, ≥99.9%), hexadecyltrimethylammonium bromide (CTAB, ≥99%), cetyltrimethylammonium chloride solution (CTAC, 25 wt% in H_2O) and hexadecylpyridinium chloride monohydrate (CPC, 99.0–102.0%) were purchased from Sigma-Aldrich. Sodium borohydride ($NaBH_4$, ≥97%), L(+)-ascorbic acid (AA, ≥99%) and silver nitrate ($AgNO_3$, ≥99%) were purchased from Roth. Potassium bromide (KBr, for IR spectroscopy) was purchased from Merck.

Synthesis of nanoparticles

Synthesis of initial seeds. Aqueous solution of $HAuCl_4$ (0.25 ml, 0.01 M) and CTAB (7.50 ml, 0.10 M) were mixed in a glass vial (50 ml) and tempered to 27 °C. 0.60 ml of 0.01 M freshly prepared, ice-cold $NaBH_4$ solution was added under vigorous stirring. The resulting solution turned brown immediately upon introduction of $NaBH_4$. The seed solution was aged for 90 min at 27 °C to ensure complete decomposition of excess borohydride.

Synthesis of spherical seeds. The synthesis of spherical seeds was adapted from Zheng *et al.*[28] In a typical synthesis, aqueous solutions of CTAC (39.00 ml, 0.10 M) and $HAuCl_4$ (1.00 ml, 0.01 M) were mixed in a glass vial (100 ml) and tempered to 27 °C in a water bath. AA (15.00 ml, 0.10 M) was added, followed by a rapid injection of 500 μl initial seeds. The solution turned red immediately and was kept at 27 °C for 15 min. The spherical seeds were collected by centrifugation at 30 000 rpm for 120 min, washed once with water and twice with 0.02 M CPC solution. The optical density of the dispersion was adjusted to 0.275 (approx. 10^{12} particles per ml). The spherical seeds were characterized by UV-Vis, TEM and AUC (Fig. S1, ESI†). Spherical seeds

with different sizes may be used for the growth of faceted particles (Fig. S3, ESI†). As a compromise of particle concentration and handling, spherical seeds from 500 μl of initial seeds were used in the following procedure.

Silver overgrowth on spherical seeds. Typically, CTAC (1.00 ml, 0.10 M), AA (0.40 ml, 0.10 M) and 1.00 ml of as prepared spherical seeds were added to water (7.00 ml). Then, $AgNO_3$ (1.00 ml, 0.01 M) was added and the mixture was heated to 65 °C and left undisturbed for 12 h.[46] The particles were collected by centrifugation (5000 rpm, 5 min).

Synthesis of faceted nanoparticles. The influence of KBr concentration, AA concentration and the number of spherical seeds was investigated. Aqueous solutions of $HAuCl_4$ (0.50 ml, 0.01 M), KBr and CPC (25.00 ml, 0.10 M) were mixed in a glass vial (100 ml) and tempered to 27 °C. An aqueous solution of AA was added, followed by a rapid injection of washed spherical seeds. The solution turned pinkish red and was kept at 27 °C for 3 h. The NPs were collected by centrifugation at 9000 rpm for 5 min and redispersed in 0.02 M CPC solution. For discrete concentrations of KBr and AA see Table S1 (ESI†).

Characterization of synthesized nanoparticles

UV-Vis spectra were recorded using a Varian Cary 50 UV-Vis Spectrophotometer. The AUC measurements were performed on an Optima XL I (Beckman Coulter, Palo Alto, CA, United States) using Rayleigh interference optics and 12 mm double sector titanium centerpieces (Nanolytics, Potsdam, Germany). A SW 60 Ti Swinging-Bucket Rotor was used at 3000 rpm and 20 °C.

The morphology and size of the synthesized NPs was observed by Scanning Electron Microscopy (SEM) and by Transmission Electron Microscopy (TEM). For electron microscopic (EM) studies, NPs were deposited on Lacey carbon or Quantifoil grids with 2 nm-thick carbon films. SEM was performed on a Zeiss Gemini 500 operating at 2 kV acceleration voltage. TEM imaging was conducted on two different instruments: a JEOL JEM-2200FS equipped with ZrO/W(100) Schottky field emission gun (operated at 200 kV) and in-column Omega-type filter and a Zeiss Libra120 with lanthanum hexaboride emitter operated at 120 kV and equipped with Koehler illumination system. The TEM images were analyzed by DigitalMicrograph (Gatan) and Fiji.[47]

The sizes, shapes, and optical properties of the synthesized NPs are shown in ESI† (Fig. S4–S10). Fig. S11 (ESI†) demonstrates the single crystalline nature of the particles as proven by electron diffraction (ED) in TEM.

Shape modelling and visualization was performed using the software VESTA.[48] The ratio of {100}, {110} and {111} facets in the NP shapes were determined based on TEM and SEM data.

The plasmonic properties of synthesized NPs were characterized by Electron Energy-Loss Spectroscopy (EELS) in a Titan3 TEM microscope operating at 80 kV. The microscope operated in the Scanning Transmission Electron Microscopy (STEM) mode (spectrum imaging) with a spatial resolution of about 1 nm. The electron beam (monochromatized by the Wien filter with an energy resolution of 70 meV) was scanned across the NPs while capturing EELSpectra that showed characteristic peaks due to surface plasmon excitations. The intensities of such peaks correlate with the probability of the excitation by the beam electrons passing through a given point in the vicinity of the particle. Correspondingly, maps of the excitation probability for various plasmon excitations were extracted. In order to simulate the plasmonic response of the NPs and their assemblies, the Maxwell's equations were solved using a boundary element approach, which worked as follows. Interfaces between media with different permittivities carry surface charges and currents at the boundary, which can be calculated in response to an external excitation (electron beam). Once the surface charges and currents are known, the induced electromagnetic fields, and in this way the excitation probability of various plasmon modes, can be derived directly. Here we used the MNPBEM toolbox as implemented by Hohenester.[49] Further details pertaining to plasmon mapping experiments and data treatment can be found in Mayer *et al.*[50]

Results and discussion

In this work we present a new synthesis procedure for single crystalline gold nanoparticles with independently tunable size and habit based on a three-step seed-mediated growth method (Fig. 1). First, small CTAB-capped gold seeds are synthesized by a procedure previously reported in many seed-mediated Au NP syntheses.[21,24,25,29,51,52] These particles are further referred to as "initial seeds". These "initial seeds" are then isotropically grown to small "spherical seeds" using the synthesis protocol adapted from Zheng *et al.*[53] It was demonstrated, that by changing the amount of "initial seeds", the size of the resulting "spherical seeds" can be adapted easily. Three different monodisperse samples (with mean diameter of 14.9 nm, 12.7 nm, and 9.5 nm) were prepared, characterized using TEM and AUC (Fig. S1, ESI†), and found to be suitable as "spherical seeds" (see Fig. S2 and S3, ESI†) for the further growth step. After a change in surfactant to CPC and adjusting the composition of growth media these "spherical seeds" are further grown to

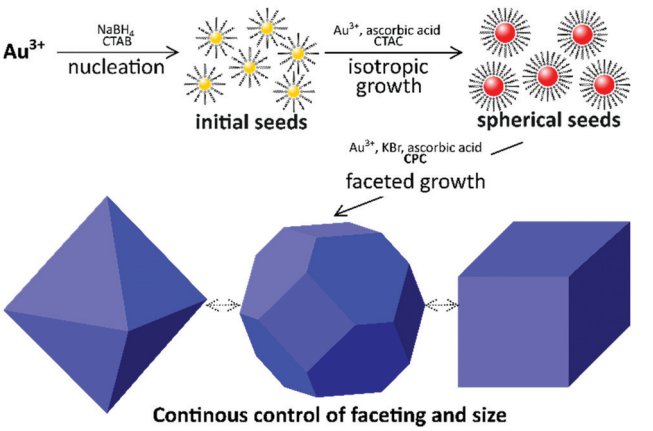

Fig. 1 Schematic representation illustrating the three-step synthesis method of faceted Au NPs. Initial small gold seeds are used to prepare single crystalline spherical seeds. These are then further grown to faceted particles with tunable ratio of the cubic {100} and octahedral {111} facets.

particles with a tunable ratio of the cubic {100} and octahedral {111} facets.

In order to develop a reliable and reproducible synthesis protocol for the synthesis of Au NPs with defined size and shape, the effect of the initial concentration of spherical seeds, KBr and AA on the reduction of gold ions and growth of NPs was examined. To exclude the effect of impurities that are present in commercially available CTAB solutions as well as side products formed during the synthesis of "spherical seeds" the growth media solution was exchanged, and initial surfactant replaced by CPC.

The size-dependency of faceted particles on the initial concentration of spherical seeds is demonstrated in detail in Fig. S4 (ESI†). Decreasing the amount of seeds 20 times leads to a particle size increase from 40 nm to 100 nm. The corresponding UV-Vis spectra of the final products are shown in Fig. S5 (ESI†), indicating the slight red shift of the SPR band with increasing particle size. Furthermore, in case the concentrations of CPC, KBr and ascorbic acid are kept constant and only the number of "spherical seeds" is varied, the bigger NPs have a cubic shape (with a low degree of truncation) while the smaller cubes are significantly more truncated by {111} facets. These results are expected since the effect of the additives should be scaled per seed concentration. Therefore, growth of specifically shaped NPs with different sizes requires both an adjustment of the amount of spherical seeds and of the remaining synthesis conditions. Particles with similar facetings with sizes between 26 nm and 100 nm can be obtained using our synthesis method (Fig. 2). We show that a low concentration of KBr in the reaction mixture leads to cubic particles

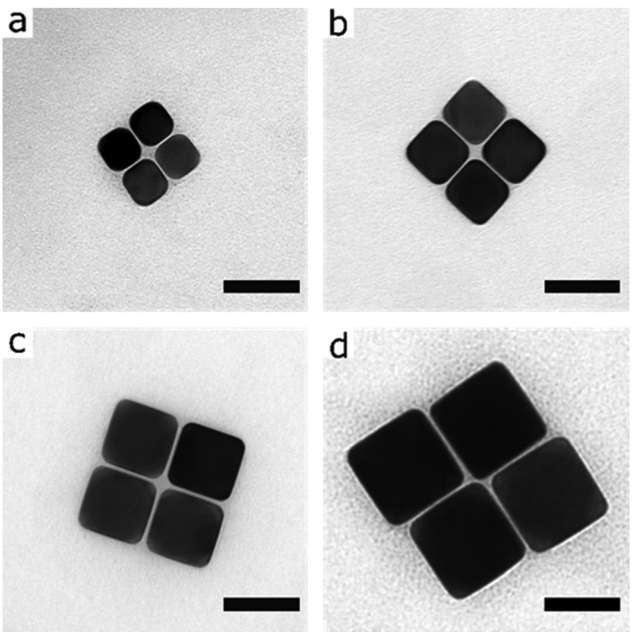

Fig. 2 Shape independent control of size of the NPs though the KBr concentration and the number of spherical seeds. Bright field TEM images of gold cubes with edge lengths of (a) 26 nm, (b) 35 nm, (c) 45 nm, (d) 61 nm. Scale bar is 50 nm for all images. UV-Vis spectra can be found in Fig. S5 (ESI†). Synthesis conditions are found in Table S1 (ESI†).

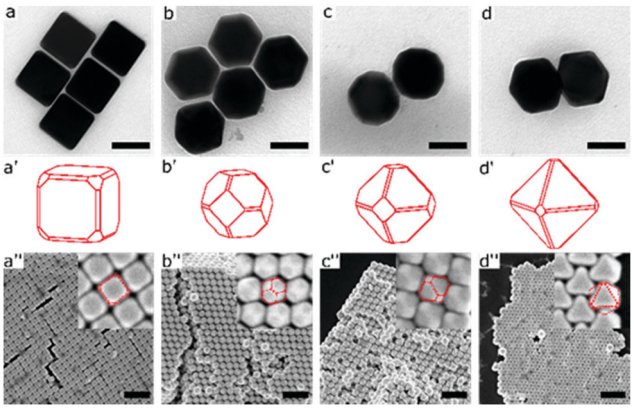

Fig. 3 Size independent control of shape of the NPs though the KBr concentration. The crystal habit of cubic {100} and octahedral {111} facets can be changed continuously while keeping the particle volume constant. The {100} facets develop more pronounced in the presence of low KBr concentrations while the {111} facets become more dominant with increasing concentrations. (a)–(d) TEM images of particles synthesized in presence of increasing KBr concentrations. Scale bar is 50 nm for all images. (a′)–(d′) Modeled shapes of the synthesized particles. The increasing truncation of the {111} facet becomes evident. (a″)–(d″) SEM images of the differently shaped particles demonstrate their neat packing behavior. A close-up with higher magnification is included, where the modeled particles are oriented as indicated by the SEM images. Scale bar is 250 nm for all images. Synthesis conditions are found in Table S1 (ESI†).

while the definition of "low" heavily depends on the initial number of spherical seeds or the final volume of the nanoparticles respectively, which is also changing the kinetics of the crystallization process (Fig. S6, ESI†). This stands in contrast to the previously reported synthesis by O'Brien *et al.*[39] where cubes with edge lengths between 43 nm and 87 nm and octahedra with edge lengths between 62 nm and 110 nm are synthesized using unchanged synthesis conditions.

With the herein presented synthesis method we are not only able to adapt the particle size, in addition we can also steplessly tune the crystal habit by adjusting the ratio of cubic {100} and octahedral {111} facets by changing the ratio of KBr and/or AA (Fig. 3, 4 and Fig. S7–S9, ESI†) while keeping the initial number of spherical seeds. The single crystalline nature of all particles was confirmed using ED (Fig. S10, ESI†). To the best of our knowledge, such procedure is not yet published for gold nanoparticles. Our study shows (Fig. 4), that Au NPs with more pronounced {100} facets develop in the presence of "low" KBr concentrations, while the {111} facets become more dominant in the NP shape with increasing KBr concentrations. If no bromide is added to the growth solution, particles without defined faceting are obtained. The increasing concentration of AA favors the formation of NPs with cubic shape. However, a broadening of the UV-Vis spectra at higher wavelengths when changing the ascorbic acid concentration indicates an increased number of oddly shaped particles. The monodispersity of size and shape of the synthesized particles is clearly demonstrated by their long-ranged assemblies (Fig. S11–S14, ESI†). The mechanism of formation and the structural characterization of such assemblies will be focus of our next publication.[54]

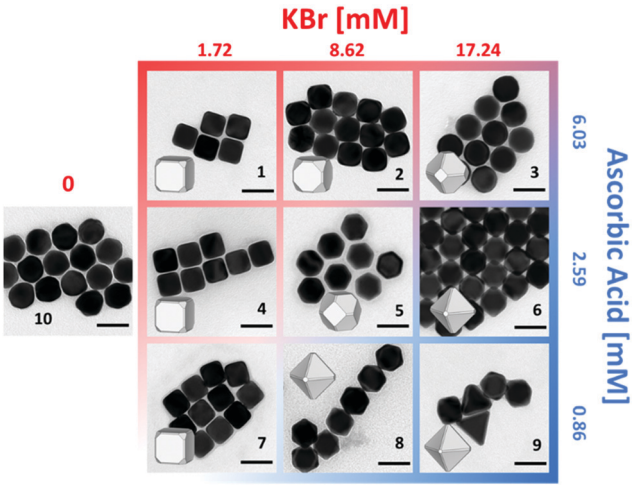

Fig. 4 (1)–(9) Bright-field TEM images of the resulting Au NPs grown at selected concentration of KBr and ascorbic acid (Table S1, ESI†). (10) Bright-field TEM image of particles grown without any addition of KBr. Scale bar is 50 nm in all images. Synthesis conditions are found in Table S1 (ESI†).

From the first glance, the observed effect of the KBr concentration on the Au NP crystal growth is very unusual and also contradicts known literature data[23,36,39] where an increased bromide concentration leads to a stronger expression of {100} facets while a lack of bromide is needed to obtain {111} facets.

In order to solve this conundrum, we performed a systematic investigation of the effect of KBr and ascorbic acid concentrations on mechanism and kinetic of Au NP growth. It is well known, that the reduction of gold ions occurs by following the consequent simplified scheme: Au(III) → Au(I) → Au^0, for our system (due to the presence of KBr and CPC and taking $HAuCl_4$ as initial salt) this can be written as: $CP[AuCl_{4-x}Br_x]$ → $CP[AuCl_{2-x}Br_x]$ → Au^0.

However, the absence of the band corresponding to the Au(III) complex in UV-Vis spectra of the growth solution indicates that the reduction of Au(III) to Au(I) proceeds very fast and prior to the NP growth process. Therefore, this step can be omitted from the evaluation of the kinetic processes. The reduction of Au(I) can proceed in two ways: [in solution: $Au(I) + 1e^- \xrightarrow{k_1} Au^0$] and [by autocatalytic surface reduction: $Au_n^0 + Au(I) + 1e^- \xrightarrow{k_2} Au_{n+1}^0$]. Without presence of initial seeds, the first process leads to fast homogeneous nucleation in solution. In our system we did not observe the presence of small particles in the TEM images, therefore we expect Au^0 to heterogeneously attach (*e.g.* nucleate) to the already existing seeds, providing further active sides for the growth process. The contribution of this process in the NP growth kinetic is very limited and therefore, growth by autocatalytic surface reduction is the most dominant process. Since, Au(I) complexes do not absorb at the recorded UV-Vis spectral range, we used the SPR band of gold nanoparticles to evaluate the kinetic of Au NP growth. The reduction kinetic of gold ions and growth of nanoparticles were studied by collecting the UV-Vis spectra of reaction solution at different time points. The detailed procedure of data collection and quantitative analysis of rate curves can be found in ESI.† Fig. S11 (ESI†) shows the normalized kinetic curves of Au NP growth at different concentrations of KBr and AA (the temperature, concentrations of CPC and "spherical seeds" are kept constant). The morphologies of the NPs obtained at selected crystallization conditions (Table S1, ESI†) are depicted in Fig. 4. The kinetic data were evaluated using the adjusted Finke–Watzky (FW) autocatalytic two-step mechanism.[40,41,43,55–57] Although, this minimalistic approach has several limitations, it allows to estimate the rate constants of the "pseudoelementary reactions" of the reduction of gold ions and growth process of Au NPs with defined shape. The rate constants k_1 and k_2 were calculated by fitting the rate curves based on a procedure described by Tatarchuk *et al.*[41,43,55]

The obtained values of k_1 and k_2 are listed in Fig. S15 and plotted *vs.* the initial concentration of KBr and AA (Fig. 5a and b) for Au NPs with different shapes. The calculated values of k_1 are significantly smaller than for k_2. It is also obvious that by increasing the KBr concentration the kinetic of the reduction process becomes slower, since complex $[AuCl_2]^-$ is less stable in comparison to $[AuCl_{2-x}Br_x]^-$ and $[AuBr_2]^-$ and has a higher redox potential (E^0 $[AuCl_2]^-$/Au = 1.154; E^0 $[AuBr_2]^-$/Au = 0.959).[58] The increasing concentration of reducing agent (AA) accelerates the reduction process. For the cubic particles, a linear dependence of k_1 and k_2 from the concentrations of KBr and AA can be shown ($R^2(k_1 = f(\text{KBr, AA})) = 0.99995$; $R^2(k_2 = f(\text{KBr, AA})) = 0.9995$). Thus, in this range of additive concentrations, the growth kinetic is mainly limited by adsorption of Br^- on the {100} facets, and inhibition of their growth, which is in consistence with previous reports.[23,36,39] Furthermore, recently it was demonstrated by MD simulations, that in contrast to Cl^- ions the Br^- ions are not only preferably adsorbing to {100}, but also reducing the surface density of surfactant micelles.[26] All these factors favor the crystallization of cubic NPs. However, in case the concentration of Br^- ions overcomes a certain value, the morphology of the cubic NPs continuously switches towards octahedral shape (Fig. 3, 4 and Fig. S7, S8, ESI†). Furthermore, the kinetic and the mechanism of crystal growth change (Fig. S15, ESI† and Fig. 5a, b). Under this condition, the $CP[AuBr_2]$ becomes the dominant species in solution, therefore it is also more likely that Br^- ions are adsorbing on the {100} facets. This $CP[AuBr_2]$ complex, similar to bromide complexes of other noble metals, has a tendency to autocatalytic surface reduction on the cubic facets, while the octahedral facets have the highest activation barrier for this process.[59] Thus, the octahedral facets grow most slowly and dominate in the final shape of the NPs. In addition, the calculated k_2 coefficients for cubic particles are significantly higher than for octahedral ones.

Last but not least, the results obtained by analysis of kinetic curves of Au NPs grown from solution with different concentration of initial spherical seeds (while keeping the same additive concentrations) are also in consistence with the proposed model (Fig. S6, ESI†). This shows that at low amounts of seeds, big cubic NPs are formed due to the fact that the selected concentration of Br^- is sufficient to efficiently inhibit

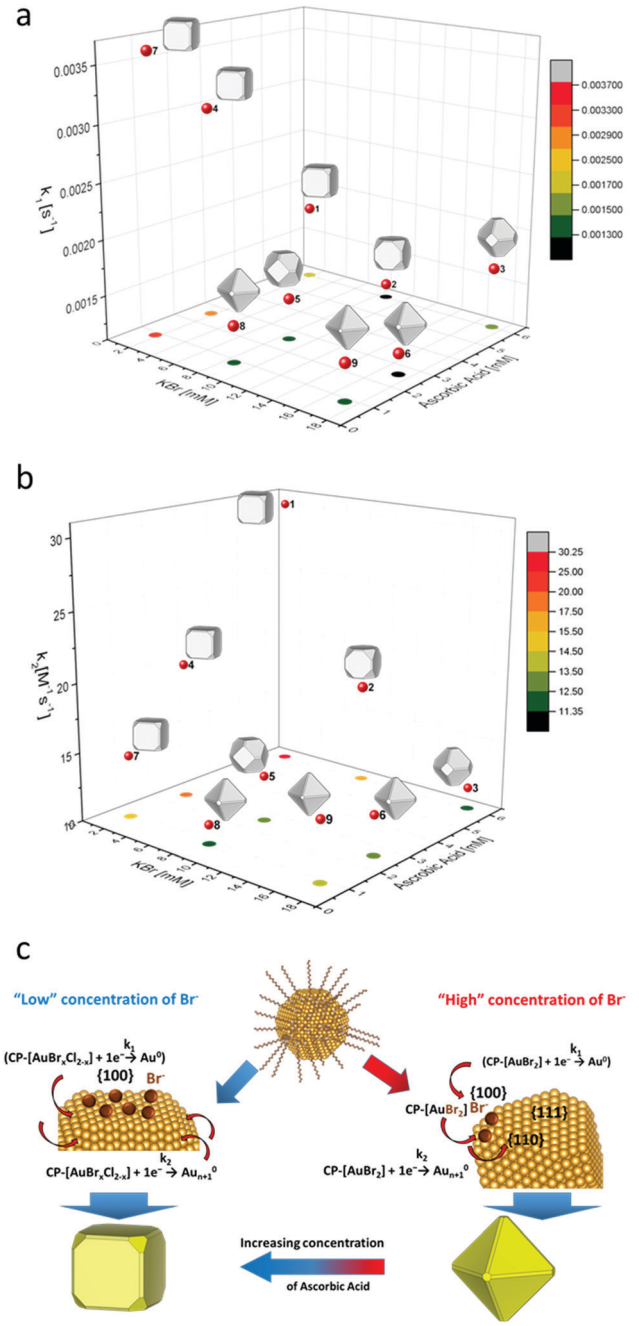

Fig. 5 The influence of KBr and AA on the reduction kinetic of gold ions and crystal growth of Au NPs. (a) and (b) Dependence of k_1 and k_2 rate constants of the "pseudoelementary" reactions on the concentrations of KBr and AA (Fig. 4 and Table S1, ESI†). The color code corresponds to the absolute values of kinetic coefficients. (c) Schematic illustration of the proposed additive controlled mechanism of the Au NP growth.

the growth of {100} faces, while the higher amount of spherical seeds yields more truncated NPs.

In summary, Fig. 5c schematically illustrates the described additive controlled mechanism of Au NP growth.

The developed synthesis technique facilitates an accurate control of size and shape of Au NPs allowing the manufacturing of nanosized structures with plasmonic properties as required

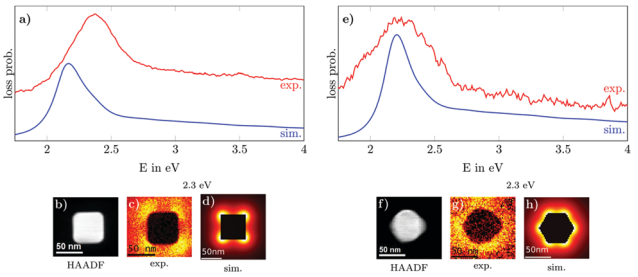

Fig. 6 Total EELSpectra of cubic (a) and octahedral (e) NPs. The corresponding High-Angular Annular Dark Field (HAADF) images obtained in the course of scanning are shown in (b), (f). A distinct peak related to the surface plasmon excitation is observed at 2.3 eV. The experimentally obtained probability maps for this excitation are shown in (c), (g) for cubic and octahedral particles, respectively. In both cases a localization of the excitation at the corners is visible. The corresponding simulated loss probability maps are shown in (d) for a cubic and in (h) for an octahedral NP. The scalebar corresponds to 50 nm, respectively.

for the various plasmonic applications (see Introduction). In order to give a prospect into this large field and to show the high quality of the synthesized NPs we finally map surface plasmon resonances of single and coupled NPs of different shapes. Fig. 6 shows the surface plasmon excitations observed in single cubic and octahedral NPs (*i.e.* the building blocks of more complex arrangements). We clearly observe a spatially localized surface plasmon in good agreement with simulations. As reported previously, the excitation probability tends to be maximal near the sharp corners of particles.[60] This localization at the corners is clearly visible in cubic particles while less pronounced in octahedral ones, probably because the corners of octahedra were a bit rounded for the investigated NPs. In principle, multiple surface plasmon modes different in energy can be excited – depending on their localization at corners, edges or facets.[61–63] For this particle size, however, we resolve these differences in neither the experiment nor the simulation, as their energies are closely centered around 2.3 eV, *i.e.* at the energy for a degenerate surface plasmon mode on single spherical Au particles.[64,65]

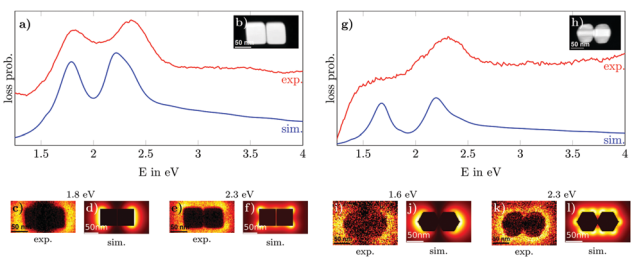

Fig. 7 Total EELSpectra of NP dimers composed of cubic (a) and octahedral (g) NPs. The corresponding High-Angular Annular Dark Field (HAADF) images obtained in the course of scanning are shown in (b), (h). Two peaks related to the surface plasmon excitations can be clearly distinguished: the basic mode at 2.3 eV and the mode associated with the correlated excitation of two particles at lower energies. The probability maps for these excitations are shown in (c), (e) for cubic and in (i), (k) for octahedral particles. The corresponding simulated loss probability maps are shown in (d), (f) for cubic and in (j), (l) for octahedral particles. The scalebar corresponds to 50 nm, respectively.

The situation is more complicated in assemblies composed of several NPs.[66] Fig. 7 exemplarily shows the plasmonic modes excited in two particles adjunct to each other (*i.e.* a NP dimer). In again good agreement with the simulated data we observed in addition to the basic mode at 2.3 eV already detected in single particles, a new (lower-energy) excitation. This mode is related to the correlative response of dielectric dipoles in two particles and is peaked at the edges of two-particles chains. A variety of long-range correlative surface plasmon excitations can be observed in longer chains.[67]

Conclusions

We have developed a three-step seed-mediated synthesis for highly monodisperse, single crystalline gold nanoparticles, allowing precise and independent control of NP size and shape. The size of the faceted particles can be tuned by adjusting the number of seeds in the synthesis procedure and the ratio of cubic {100} and octahedral {111} facets can be steplessly adjusted by changing the ratio of seeds, KBr and ascorbic acid in the synthesis procedure. The ability of Au NPs to form long-range assemblies are used to illustrate their extraordinary quality. Au NP with more pronounced {100} facets evolve in the presence of "low" KBr concentrations, while the {111} facets become more dominant with increasing bromide concentrations. The effect of ascorbic acid on the morphology of NPs is less pronounced, but its higher concentration favors the formation of cubic NPs. As this seems to contradict previously published syntheses, the influence of the bromide and AA concentration on the kinetics was systematically investigated. The kinetic data were evaluated using the minimalistic Finke–Watzky autocatalytic two-step mechanism and it is found that for low bromide concentrations, the growth kinetic is mainly limited by adsorption of Br^- on the {100} facets. For higher bromide concentrations autocatalytic surface reduction of $[AuBr_2]^-$ complex on the cubic facets becomes dominant and octahedral facets evolve in the final shape of the NPs. Based on these data, a surface-mediated mechanism of gold ions reduction and Au NPs growth is proposed, which allows to explain the effect of gradual increase of bromide ions concentration on switching the Au NPs morphology from cubic to octahedral. The plasmonic response of single particles and their assemblies is demonstrated employing spatially resolved EELS. For single particles we find the spatially localized surface plasmon in good agreement with simulations around 2.3 eV. Assemblies (*e.g.* NPs dimers) exhibit an additional (lower-energy) excitation that is related to the correlative response of dielectric dipoles in two particles. The accurate control of the particle morphology allows manufacturing nanostructured materials with desired plasmonic properties.

Conflicts of interest

There are no conflicts to declare.

Acknowledgements

The authors appreciate support from ERC (grant 715620 under the Horizon 2020 program), DFG funded SFB1214 (project B1) and DFG EXC2147/1 ST0232019 project under Germany's Excellence Strategy – "Cluster of Excellence on Complexity and Topology in Quantum Matter – ct.qmat". The authors thank Prof. Alexander Wittemann, Dr Marina Krumova, Rose Rosenberg, Dirk Haffke for experimental support and fruitful discussions. G. G.-R. acknowledges the Alexander von Humboldt Foundation for financial support. E. S. thank the Zukunftskolleg at the University of Konstanz for financial support.

References

1 C. Matricardi, C. Hanske, J. L. Garcia-Pomar, J. Langer, A. Mihi and L. M. Liz-Marzan, *ACS Nano*, 2018, **12**, 8531–8539.
2 Z. Zhu, H. Meng, W. Liu, X. Liu, J. Gong, X. Qiu, L. Jiang, D. Wang and Z. Tang, *Angew. Chem., Int. Ed.*, 2011, **50**, 1593–1596.
3 E. Priyadarshini and N. Pradhan, *Sens. Actuators, B*, 2017, **238**, 888–902.
4 G. Liu, M. Lu, X. Huang, T. Li and D. Xu, *Sensors*, 2018, **18**, 4166.
5 Y. F. Huang, Y. W. Lin, Z. H. Lin and H. T. Chang, *J. Nanopart. Res.*, 2009, **11**, 775–783.
6 M. Pastuszczak and A. Wojas-Pelc, *Postepy Dermatol Alergol*, 2013, **30**, 203–210.
7 H. Kaur, B. R. Babu and S. Maiti, *Chem. Rev.*, 2007, **107**, 4672–4697.
8 S. Kutrovskaya, A. Kucherik, A. Osipov, V. Samyshkin, A. Istratov and A. V. Kavokin, *Sci. Rep.*, 2019, **9**, 7023.
9 M. Kobayashi, S. Tomita, K. Sawada, K. Shiba, H. Yanagi, I. Yamashita and Y. Uraoka, *Opt. Express*, 2012, **20**, 24856–24863.
10 T. H. Ha, H. J. Koo and B. H. Chung, *J. Phys. Chem. C*, 2007, **111**, 1123–1130.
11 L. Garcia-Cruz, V. Montiel and J. Solla-Gullon, *Chem. Nanomater.*, 2019, **1**, 103–156, DOI: 10.1515/9783110345100-003.
12 C. Burda, X. Chen, R. Narayanan and M. A. El-Sayed, *Chem. Rev.*, 2005, **105**, 1025–1102.
13 V. Amendola, R. Pilot, M. Frasconi, O. M. Marago and M. A. Iati, *J. Phys.: Condens. Matter*, 2017, **29**, 203002.
14 K. L. Kelly, E. Coronado, L. L. Zhao and G. C. Schatz, *J. Phys. Chem. B*, 2003, **107**, 668–677.
15 M. Mayer, A. M. Steiner, F. Roder, P. Formanek, T. A. F. Konig and A. Fery, *Angew. Chem., Int. Ed.*, 2017, **56**, 15866–15870.
16 E. V. Sturm and H. Colfen, *Crystals*, 2017, **7**, 207.
17 D. V. Talapin and E. V. Shevchenko, *Chem. Rev.*, 2016, **116**, 10343–10345.
18 M. Grzelczak, J. Perez-Juste, P. Mulvaney and L. M. Liz-Marzan, *Chem. Soc. Rev.*, 2008, **37**, 1783–1791.
19 J. Kimling, M. Maier, B. Okenve, V. Kotaidis, H. Ballot and A. Plech, *J. Phys. Chem. B*, 2006, **110**, 15700–15707.
20 J. Turkevich, P. C. Stevenson and J. Hillier, *Discuss. Faraday Soc.*, 1951, **11**, 55–75.

21 N. R. Jana, L. Gearheart and C. J. Murphy, *Adv. Mater.*, 2001, **13**, 1389–1393.
22 C. J. Murphy, T. K. Sau, A. M. Gole, C. J. Orendorff, J. Gao, L. Gou, S. E. Hunyadi and T. Li, *J. Phys. Chem. B*, 2005, **109**, 13857–13870.
23 W. Niu, S. Zheng, D. Wang, X. Liu, H. Li, S. Han, J. Chen, Z. Tang and G. Xu, *J. Am. Chem. Soc.*, 2009, **131**, 697–703.
24 B. Nikoobakht and M. A. El-Sayed, *Chem. Mater.*, 2003, **15**, 1957–1962.
25 X. Ye, L. Jin, H. Caglayan, J. Chen, G. Xing, C. Zheng, V. Doan-Nguyen, Y. Kang, N. Engheta, C. R. Kagan and C. B. Murray, *ACS Nano*, 2012, **6**, 2804–2817.
26 S. K. Meena, S. Celiksoy, P. Schafer, A. Henkel, C. Sonnichsen and M. Sulpizi, *Phys. Chem. Chem. Phys.*, 2016, **18**, 13246–13254.
27 K. X. Yao, X. M. Yin, T. H. Wang and H. C. Zeng, *J. Am. Chem. Soc.*, 2010, **132**, 6131–6144.
28 Y. Zheng, Y. Ma, J. Zeng, X. Zhong, M. Jin, Z. Y. Li and Y. Xia, *Chem. – Asian J.*, 2013, **8**, 792–799.
29 T. K. Sau and C. J. Murphy, *J. Am. Chem. Soc.*, 2004, **126**, 8648–8649.
30 S. Si, C. Leduc, M. H. Delville and B. Lounis, *ChemPhysChem*, 2012, **13**, 193–202.
31 S. E. Lohse, N. D. Burrows, L. Scarabelli, L. M. Liz-Marzan and C. J. Murphy, *Chem. Mater.*, 2014, **26**, 34–43.
32 R. G. Rayavarapu, C. Ungureanu, P. Krystek, T. G. van Leeuwen and S. Manohar, *Langmuir*, 2010, **26**, 5050–5055.
33 D. K. Smith and B. A. Korgel, *Langmuir*, 2008, **24**, 644–649.
34 N. Almora-Barrios, G. Novell-Leruth, P. Whiting, L. M. Liz-Marzan and N. Lopez, *Nano Lett.*, 2014, **14**, 871–875.
35 A. Gole and C. J. Murphy, *Chem. Mater.*, 2004, **16**, 3633–3640.
36 M. R. Langille, M. L. Personick, J. Zhang and C. A. Mirkin, *J. Am. Chem. Soc.*, 2012, **134**, 14542–14554.
37 W. Niu, Y. A. Chua, W. Zhang, H. Huang and X. Lu, *J. Am. Chem. Soc.*, 2015, **137**, 10460–10463.
38 C. G. Khoury and T. Vo-Dinh, *J. Phys. Chem. C*, 2008, 18849–18859.
39 M. N. O'Brien, M. R. Jones, K. A. Brown and C. A. Mirkin, *J. Am. Chem. Soc.*, 2014, **136**, 7603–7606.
40 A. P. Sergievskaya, V. V. Tatarchuk, E. V. Makotchenko and I. V. Mironov, *J. Mater. Res.*, 2015, **30**, 1925–1933.
41 V. V. Tatarchuk, Y. O. Dobrolyubova, I. A. Druzhinina, V. I. Zaikovskii, P. N. Gevko, E. A. Maksimovskii and S. A. Gromilov, *Russ. J. Inorg. Chem.*, 2016, **61**, 535–543.
42 V. V. Tatarchuk, A. P. Sergievskaya, I. A. Druzhinina and V. I. Zaikovsky, *J. Nanopart. Res.*, 2011, **13**, 4997.
43 V. V. Tatarchuk, A. P. Sergievskaya, T. M. Korda, I. A. Druzhinina and V. I. Zaikovsky, *Chem. Mater.*, 2013, **25**, 3570–3579.
44 M. A. Watzky and R. G. Finke, *J. Am. Chem. Soc.*, 1997, **119**, 10382–10400.
45 M. A. Watzky and R. G. Finke, *ACS Omega*, 2018, **3**, 1555–1563.
46 S. Gómez-Graña, B. Goris, T. Altantzis, C. Fernández-López, E. Carbó-Argibay, A. Guerrero-Martínez, N. Almora-Barrios, N. López, I. Pastoriza-Santos, J. Pérez-Juste, S. Bals, G. Van Tendeloo and L. M. Liz-Marzán, *J. Phys. Chem. Lett.*, 2013, **4**, 2209–2216.
47 J. Schindelin, I. Arganda-Carreras, E. Frise, V. Kaynig, M. Longair, T. Pietzsch, S. Preibisch, C. Rueden, S. Saalfeld and B. Schmid, *Nat. Methods*, 2012, **9**, 676–682.
48 K. Momma and F. Izumi, *J. Appl. Crystallogr.*, 2011, **44**, 1272–1276.
49 U. Hohenester, *Comput. Phys. Commun.*, 2014, **185**, 1177–1187.
50 M. Mayer, P. L. Potapov, D. Pohl, A. M. Steiner, J. Schultz, B. Rellinghaus, A. Lubk, T. A. F. Konig and A. Fery, *Nano Lett.*, 2019, **19**, 3854–3862.
51 G. Gonzalez-Rubio, V. Kumar, P. Llombart, P. Diaz-Nunez, E. Bladt, T. Altantzis, S. Bals, O. Pena-Rodriguez, E. G. Noya, L. G. MacDowell, A. Guerrero-Martinez and L. M. Liz-Marzan, *ACS Nano*, 2019, **13**, 4424–4435.
52 G. Gonzalez-Rubio, T. M. de Oliveira, T. Altantzis, A. La Porta, A. Guerrero-Martinez, S. Bals, L. Scarabelli and L. M. Liz-Marzan, *Chem. Commun.*, 2017, **53**, 11360–11363.
53 L. Zhou and P. O'Brien, *J. Phys. Chem. Lett.*, 2012, **3**, 620–628.
54 J. Carnis, F. Kirner, Y. Y. Kim, R. Kubbhutdinov, A. Ignatenko, E. Iashina, A. Mistonov, T. Steegemans, S. Lazarev, M. Sprung, S. Sturm, E. Sturm and I. Vartaniants, unpublished work.
55 V. V. Tatarchuk, A. P. Sergievskaya, I. A. Druzhinina and V. I. Zaikovsky, *J. Nanopart. Res.*, 2011, **13**, 4997–5007.
56 M. A. Watzky and R. G. Finke, *J. Am. Chem. Soc.*, 1997, **119**, 10382–10400.
57 M. A. Watzky and R. G. Finke, *ACS Omega*, 2018, **3**, 1555–1563.
58 Y. Holade, D. P. Hickey and S. D. Minteer, *J. Mater. Chem. A*, 2016, **4**, 17154–17162.
59 X. Yang, C. Liu, Y. Li, F. Marchesoni, P. Hänggi and H. P. Zhang, *Proc. Natl. Acad. Sci. U. S. A.*, 2017, **114**, 9564–9569.
60 J. Nelayah, M. Kociak, O. Stéphan, F. J. García de Abajo, M. Tencé, L. Henrard, D. Taverna, I. Pastoriza-Santos, L. M. Liz-Marzán and C. Colliex, *Nat. Phys.*, 2007, **3**, 348–353.
61 J. Nelayah, M. Kociak, O. Stephan, F. J. G. de Abajo, M. Tence, L. Henrard, D. Taverna, I. Pastoriza-Santos, L. M. Liz-Marzan and C. Colliex, *Nat. Phys.*, 2007, **3**, 348–353.
62 B. Schaffer, K. Riegler, G. Kothleitner, W. Grogger and F. Hofer, *Micron*, 2009, **40**, 269–273.
63 A. Hörl, A. Trügler and U. Hohenester, *ACS Photonics*, 2015, **2**, 1429–1435.
64 B. Schaffer, K. Riegler, G. Kothleitner, W. Grogger and F. Hofer, *Micron*, 2009, **40**, 269–273.
65 A. Derkachova, K. Kolwas and I. Demchenko, *Plasmonics*, 2016, **11**, 941–951.
66 S. J. Barrow, S. M. Collins, D. Rossouw, A. M. Funston, G. A. Botton, P. A. Midgley and P. Mulvaney, *ACS Nano*, 2016, **10**, 8552–8563.
67 S. J. Barrow, D. Rossouw, A. M. Funston, G. A. Botton and P. Mulvaney, *Nano Lett.*, 2014, **14**, 3799–3808.